Wave energy conversion under constrained wave-by-wave impedance matching with amplitude and phase-match limits

Umesh A. Korde[a,*]

[a]*Environmental Health and Engineering Department, Johns Hopkins University, Baltimore, MD 21218, USA.*

Abstract

This paper investigates an approach to limit the fullness of 'tuning' provided by wave-by-wave impedance matching control of wave energy devices in irregular waves. A single analytical formulation based on the Lagrange multiplier approach of Evans (1981) [1] is used to limit the velocity amplitude while also limiting the closeness of the phase match between velocity and exciting force. The paper studies the effect of the present technique in concurrently limiting the device velocity and the required control/actuation force. Time domain application requires wave-profile prediction, which here is based on a deterministic propagation model. Also examined in the time domain is the effect of possible violation of the displacement constraint, which for many designs implies impacts at hard stops within the power take-off mechanism. Time domain simulations are carried out for a 2-body axisymmetric converter (with physical end-stops) in sea states reported for a site off the US east coast. It is found that the approach leads to effective power conversion in the less energetic sea states, while as desired, considerable muting of the optimal response is found in the larger sea states. Under the assumptions of this work, the end-stop collisions are found to have a minor effect on the power conversion. The present approach could be used to guide the design of power take-off systems so that their displacement stroke, maximum force, and resistive and reactive power limits are well-matched to the achievable performance of a given controlled primary energy converter.

Keywords: Wave energy conversion; constrained impedance-matching control; wave-by-wave control; relative oscillation; time-domain; irregular waves, displacement and force constraints; end stops.

*Corresponding author
Email address: ukorde1@jhu.edu (Umesh A. Korde)

Nomenclature

α Actuator stroke limit $\leq$ device excursion limit

α_b Bottom taper angle describing the oceanographic-buoy profile

$\beta(i\omega)$ Complex velocity constraint for frequency ω

λ Lagrange multiplier

$\lambda_1(\omega), \lambda_2(\omega)$ Parameters associated with resistive and reactive loads, respectively, at frequency ω

θ_f Forced phase error in order to meet displacement/force constraints

$a(\omega)$ Fourier transformable part of the frequency-dependent added mass at ω; $a(\omega) = \overline{a}(\omega) - \overline{a}(\infty)$

$A(i\omega)$ Complex wave amplitude (i.e., includes amplitude and phase)

$b(\omega)$ Radiation damping due to device oscillations at frequency ω

$C(\omega)$ Reactive part of the device impedance at frequency ω

c_d Linearized viscous friction damping

D Damping load applied by power take-off actuator with just adjustable resistive loading

d Distance between up-wave measurement point x_A and device centroid location x_B

$F_f(i\omega)$ Diffraction force , i.e. 'exciting' force in the presence of waves at frequency ω

$F_L(i\omega)$ Force to be applied by the actuator system at frequency ω

$F_{L1}(i\omega)$ Resistive part of the actuator force at frequency ω

$F_{L2}(i\omega)$ Reactive part of the actuator force at frequency ω

H_f Complex exciting force amplitude per unit amplitude frequency variation

$h_l(t)$ Impulse response function representing the wave propagation model

H_o Velocity frequency response under present optimal constrained control

$h_o(t)$ Impulse response function with constrained impedance matching control

$h_r(t)$ Radiation impulse response function

H_s Significant wave height

k Stiffness coefficient opposing oscillation (hydrostatic for heave, pitch, etc.

L_w Wave length in regular waves

m In-air mass of the device

$P_a(\omega)$ Maximum reactive power exchanged with device at frequency ω

$P_w(\omega)$ Mean converted power at frequency ω

P_{oe} Power converted with end-stop collisions occurring

T_e Energy period

$U(i\omega)$ Complex amplitude of oscillation velocity at frequency ω

$u_e(t)$ Cumulative impact-caused velocity, added to each time an end-stop collision occurs

$u_o(t)$ Velocity in the time domain under constrained impedance matching control

U_o, U_e, U_{es} Fourier transforms of velocities u_o, u_e, and u_{es} respectively.

U_r, U_i Real and imaginary parts, respectively, of velocity $U(i\omega)$

$u_{oe}(t)$ Velocity with end-stop collisions occurring

x_A Point of up-wave wave profile measurement

x_B Device centroid location

$\mathcal{F}_C$ Limiting reactive force practical with the actuator

$\mathcal{F}_R$ Limiting resistive force practical with the actuator

$\mathcal{F}_{lm}$ Total limiting force practical with the actuator

$\overline{a}(\infty)$ Infinite-frequency added mass in the device oscillation mode

$\overline{P}_c(\omega)$ Wave power converted during a cycle at frequency ω

1. Introduction

While attempts to use wave energy have been reported since the late 18th century (e.g. [2]), serious efforts to utilize ocean waves for large scale energy generation began with the work of Salter [3]. Optimum energy conversion required large devices, posing serious design challenges [4], [5]. However, smaller devices such as heaving axisymmetric buoys that utilized favorable 3-dimensional interactions with incoming waves also began to be developed in the 1970's [6]. To reach the theoretically attractive energy conversion levels [e.g. heaving axisymmetric buoys in regular waves enabling capture widths reaching $\sim L_w/(2\pi)$ (L_w being the wave length)], small devices often required oscillation amplitudes that could not be supported by the device components. Frequency domain solutions for optimum velocities under displacement/velocity constraints were derived by Evans [1] for single and multiple small devices in an array. To expand the bandwidths of efficient energy conversion, control techniques

to force resonant oscillations with reactive loading (in addition to the power absorbing resistive loads) were developed in the late 1970's [6], [7]. For small axisymmetric heaving buoys, an alternative switching/latching control was also developed [8]. Whereas latching type phase control approaches required large braking forces, direct reactive control via spring and inertia loads required large forces for small devices in long swells.

Control for optimum conversion under motion constraints was investigated for multi-element arrays in [9], and for multi-mode devices (≥ 2) in [10] as well as [11]. It does not appear that similar solutions were explored for the constraining actuation forces, arguably because latching control received more attention in the ensuing decades, and large braking forces were considered less problematic than large continuously varying forces. Explicit application of force constraints in an *a posteriori* manner (i.e. following constrained optimization with displacement limits) was considered in [12], so that the model predictive control based solution satisfying motion constraints did not need actuator forces exceeding the prescribed force limits. Other applications of model predictive control to enforce displacement and force limits include [13], and more recently, the laboratory experiments reported in [14]. Combined use of force and displacement inequality constraints within a single time-domain formulation was reported in [15], [16], where the motion and force variables were discretized via Fourier decomposition in terms of sine and cosine and functions, and constraint selection was guided by a geometric interpretation of the actuator force, exciting force, and displacement.

The goal of this work is to investigate an approach for combining force and displacement limits within a single analytical formulation, for use in wave-by-wave[1] impedance matching control based on a wave-elevation time-series predicted some seconds into the future. Under suitable approximations, the predictions enable acausal impulse response functions to be used to determine actuator forces that drive the device velocity to be approximately synchronous with the exciting force (in frequency-domain, this would correspond to a phase-match between exciting force and device velocity over a broad range of frequencies), while maintaining an energy absorption rate that approximately equals the energy radiation rate. Recent work on such control included just displacement/velocity constraints designed using the frequency domain formulation of [1], as discussed in [17], [18], and [19]. It was found that for small devices in swell-dominated seas, the maximum reactive forces and powers

[1] A wave in the phrase 'wave-by-wave' is here understood to be the free-surface motion from one zero up-crossing to the next, in an irregular wave input approaching the device.

became considerably larger than the maximum resistive forces and mean converted powers. The present work examines an analytical approach to enforce force limits in a manner resembling the way displacement constraints are applied, so that both constraints can be prescribed *a priori* at the start, and solutions lying on their defining envelopes can be evaluated under real-time wave-by-wave constrained impedance matching control. It should be pointed out that the approach of [1] 'globalizes' the constraint for multiple-mode conversion. For this reason, the proposed extension in its present form is limited to single-mode or single-mode reducible devices, such as the 2-body axisymmetric system considered later. It is recognized that the frequency-domain constraint specification does not guarantee constraint satisfaction in the time domain for arbitrary sea states, and hence the time-domain solutions need to be reviewed in each case. Nonetheless, it appears that the present approach could provide quick and useful information for power take-off design/selection early in the device design process.

It should be noted that power conversion is large in sea states conducive to the device natural response (i.e., dominant periods close to the device resonant period), and the actuator force is dominated by the resistive part with the reactive force/powers being small. Away from resonance, for small devices, the reactive forces can be the dominant force component (just to provide impedance matching) with the resistive force still needing to be large for the purpose of displacement-constraint satisfaction. In such cases, the reactive powers can be very large (i.e. large maxima, even though the net reactive power absent power take-off dissipation is zero), and can challenge the limits of the power take-off and available energy storage systems. The overall forces can also prove too large for a single actuator. For these reasons, it seems reasonable to ask whether both reactive and resistive forces could be reduced while still meeting displacement constraints and maintaining sufficiently large power conversion, through a slight intentional detuning of the optimum control force. Note that in an analytical frequency domain formulation for purely displacement/velocity constraints, the Lagrange multiplier has the significance of an added constraint-enforcing damping. Here an additional Lagrange multiplier is introduced, to serve as the reactive detuning load. It is argued that the two Lagrange multipliers could help to restrict velocity/displacement amplitudes and limit reactive loads, by constraining the extent of the exciting force-velocity phase match to a value $\theta_f > 0$. The automatic reduction in velocity caused by deliberate detuning would further mitigate the need for large resistive loads. The effect of detuning here is to 'flatten the peak'. The reduction in

converted power is accompanied by a reduction in the control/actuation force magnitudes. Because the detuning can be controlled, this approach would add a degree of convenience to the overall operation of the device in changing wave conditions. It should be added that the term 'detuning' here is used somewhat differently than in [20], where the term is used to represent an increase in bandwidth via reactive control.

The displacement limits in this work are thought to be governed by actuator stroke limits rather than the maximum device excursion possible, as it is expected that actuator strokes would frequently be smaller than the maximum excursion allowed by the device geometry. Since, for most actuators the force and stroke limits are embedded in the actuator hardware design, known relations exist between the maximum stroke and maximum force, and can be used in the present formulation to evaluate a range of device and actuator sizes. Analytical formulations such as investigated in the present work could be considered helpful in the early overall design and development stages for the device. Alternatively, the force-displacement limits using this approach (in a range of expected sea states) could be utilized to design a custom actuator system for practical application.

Because the constraints here are prescribed within a frequency domain formulation and then transformed into a time-domain formulation leading to implementation, the constraints may be exceeded in the time domain in response to some sea states. The effect of such constraint violations is also investigated here, for a set of applications where actuator strokes are physically limited by the hardware. Such limits are here referred to as 'end stops'. The effect of collisions between the moving elements and the reference occurring each time the constraint is violated is modeled here in the time domain, and the changes in device velocity and converted power are also evaluated. It should be mentioned that end stop avoidance has been a crucial design goal in wave energy for several decades (e.g. see, [21], [22]), and it may be possible in practice to avoid physical impacts at actuator limits through careful design. This work supposes that the actuators being used here are off-the-shelf hydraulic cylinders or custom hydraulic cylinders with topologies resembling most off-the-shelf cylinders. It is likely that the stroke limit problem may also exist in the case of electromechanical actuators, as discovered in recent experimental work [23].

Finally, it is noted that the device employed in this work is intended to represent a class of mid-size oceanographic buoys (hence the proposed size and geometry) supporting sensor packages on board and on moorings (e.g. [24]. The goal, therefore, is to maximize power conversion with

retrofitted realistic actuators in a range of wave conditions expected at proposed deployment sites where ocean-variable measurements are desired. However, the cost/economic considerations for such retro-fitted implementations are considerably different from those associated with dedicated wave energy converters. Device dimensions here are constrained to allow wave-power integration into existing oceanographic buoys. Section 2 following this introduction describes the constraint formulation in the frequency domain, as well as its resulting time-domain counterpart. Section 3 outlines the time domain procedure used here to quantify the effect of end-stop collisions at the actuator between the oscillating elements of the device. Section 4 summarizes the calculations and time-domain simulations carried out here and the results sought. Section 5 discusses the results and points out some of the major findings, while Section 6 outlines the principal outcomes of this work that could be of potential use in applications. Appendix 1 briefly outlines the frequency and time-domain models for the device geometry considered in this work, while, for completeness, Appendix 2 outlines the wave prediction approach. The material in both Appendix sections has appeared elsewhere, and is referenced where relevant.

2. Formulation

Two-body axisymmetric concentric heaving bodies have been of interest since the work of Budal and Falnes [25]. Such devices are of relevance to this work given its possible application in oceanographic measurements, as indicated in Section 1. The particular manifestation chosen for the application example and calculations included in this paper is shown in Figure 1, wherein the surface-floating body is a mid-size oceanographic buoy and the the space between the two concentric submerged discs is used to support instrumentation. Considered below is a single mode device or systems such as two axisymmetric concentric bodies in heave that can be reduced to an equivalent single-mode device. The quantities below are related to their counterparts in an equivalent single-mode model for a two-body axisymmetric system. These relations are summarized in Appendix 1. Small amplitude waves and small-amplitude oscillations are assumed in the treatment below. For frequency-domain quantities such as velocity $U(i\omega)$ below, the argument $i\omega$ is preserved through the steps to indicate that the quantity represented is complex, with an amplitude and a phase. Small amplitude waves and small-amplitude oscillations are assumed in the treatment below. In terms of the mechanical actuation system, it is supposed that the actuator is chosen or designed such that its stroke α is less than the maximum displacement of the floating body without fully emerging above

or submerging below the free surface [8]. The actuator stroke limit therefore constrains the device velocity according to,

$$|U(i\omega)| \leq |\beta(i\omega)| = i\omega\alpha. \tag{1}$$

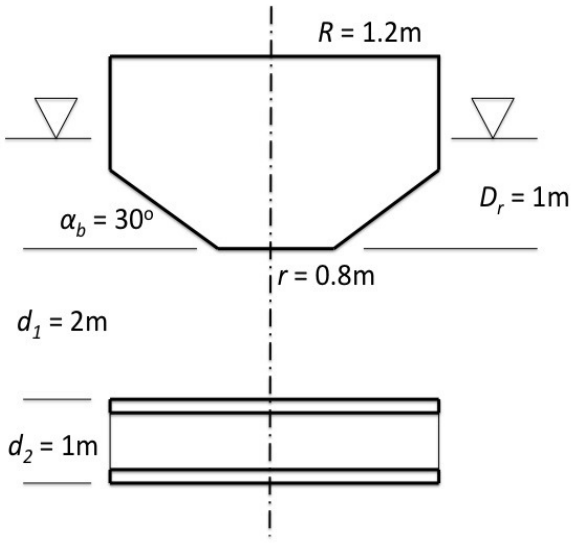

Figure 1: The 2-body axisymmetric converter studied in this work. Relative heave oscillation is used in energy conversion, and the equations of motion can rearranged in terms of the relative oscillation so that the relative heave dynamics can be understood using a single-mode framework. The buoy radius matches that of a mid-size oceanographic buoy. The space between the two submerged concentric discs may be used to support oceanographic sensors.

As a background to the following discussion, the original velocity constraint treatment of Evans [1] is summarized below. $F_f(i\omega)$ below represents the exciting force per unit wave amplitude.

$$\overline{P}_c(\omega) = \frac{1}{4}\left[F_f(i\omega)U_i^*(i\omega) + U(i\omega)F_f^*(i\omega)\right] - \frac{1}{2}U(i\omega)b(\omega)U^*(i\omega) - \frac{1}{2}\lambda\left[U(i\omega)U^*(i\omega) - \beta^2\right], \tag{2}$$

where λ is a Lagrange multiplier to be determined along with the constrained optimum velocity $U_c(i\omega)$. Realizing that absorbed power under velocity constraint in equation (2) for a chosen frequency ω has an explicit dependence on U, U^*, and λ, a small variation $\delta\overline{P}_c$ can be expressed as,

$$\delta\overline{P}_c = \frac{\partial\overline{P}_c}{\partial U}\delta U + \frac{\partial\overline{P}_c}{\partial U^*}\delta U^* + \frac{\partial\overline{P}_c}{\partial\lambda}\delta\lambda, \tag{3}$$

where the arguments ω or $i\omega$ have temporarily been dropped to keep the notation from getting cumbersome. When $\overline{P}_c$ is maximum, i.e. at a 'peak', an infinitesimal move in any 'direction' about

the peak causes no change in $\overline{P}_c$, or $\delta\overline{P}_c = 0$. For this to be true for any direction,

$$\frac{\partial \overline{P}_c}{\partial U} = \frac{\partial \overline{P}_c}{\partial U^*} = \frac{\partial \overline{P}_c}{\partial \lambda} = 0. \tag{4}$$

The first two relations lead to the conditions,

$$\begin{aligned} &\frac{1}{2}F_f^*(i\omega) - b(\omega)U^*(i\omega) - \lambda U^*(i\omega) = 0, \\ &\frac{1}{2}F_f(i\omega) - U(i\omega)b(\omega) - U(i\omega)\lambda = 0. \end{aligned} \tag{5}$$

The second of the two equations in (5) provides an expression for the optimum velocity $U_c(i\omega)$ under the given constraint,

$$U_c(i\omega) = \frac{F_f(i\omega)}{2[b(\omega) + \lambda]}. \tag{6}$$

The Lagrange multiplier $\lambda(\omega)$ is thus found to have the significance of additional damping λ that the power take-off can apply to push the load over optimum damping, so that now $D = b(\omega) + \lambda$. The additional damping λ can also be applied by a method exterior to the power take-off, but it is assumed here to be provided by the power take-off. To find the correct value of λ, it is argued that since at the 'constrained optimum', $U_c(i\omega) = \beta(\omega)$ (both β and so λ may be given a frequency dependence), using equation (6) and some algebra it is found that

$$\lambda(\omega) = \frac{|F_f(i\omega)|}{2\beta(\omega)} - b(\omega). \tag{7}$$

It is possible that close to resonance, the λ required to restrict oscillations to within the oscillation constraint is so large that the force required of the power take-off force exceeds the mechanical force limits. Further, when active impedance matching is sought via reactive loading, for small devices the reactive force requirement may also be so large as to exceed the power take-off force limits, either by itself or in combination with the required resistive force due to λ. In the treatment below, two quantities, λ_1 and λ_2 are defined, where λ_1 has the significance of a resistive load, and λ_2 has the significance of a reactive load. In some cases, the resistive and reactive components may be applied by different actuators; however, this is by no means a necessary condition for the following analysis. The total actuator force may be expressed as,

$$F_L(i\omega) = F_{L1}(i\omega) + F_{L2}(i\omega), \tag{8}$$

where,

$$F_{L1}(i\omega) = [b(\omega) + \lambda_1(\omega)]\, U(i\omega), \text{and,}$$
$$F_{L2}(i\omega) = i\,[\lambda_2(\omega) - C(\omega)]\, U(i\omega). \tag{9}$$

Here, $b(\omega)$ is the radiation damping, $C(\omega)$ the reactive impedance, and $\lambda_1(\omega)$ and $\lambda_2(\omega)$ are parameters to be determined. The linearized viscous damping c_d is ignored here. The reactive impedance can be seen to be,

$$C(\omega) = \omega\,[m + \overline{a}(\infty) + a(\omega)] - k/\omega. \tag{10}$$

Here m is the in-air mass of the device, $\overline{a}(\infty)$ is the infinite-frequency added mass, and $a(\omega)$ is just the frequency-variable added mass. k is the stiffness providing the restoring force for oscillation. $\overline{a}(\infty)$ and $a(\omega)$ are defined for the particular translational oscillation mode being considered. k represents the hydrostatic stiffness in the case of heave, but may be provided by mooring cables or by the actuator system itself in the case of surge and sway oscillation modes. The magnitude limits on the two force components in equation (9) may be constrained as follows. First,

$$|[b(\omega) + \lambda_1(\omega)]\, U(i\omega)| \leq |\mathcal{F}_R|\,, \tag{11}$$

where $\mathcal{F}_R$ denotes the limiting resistive force practical with the actuator(s). For the reactive force,

$$|[\lambda_2(\omega) - C(\omega)]|\,|U(i\omega)| \leq |\mathcal{F}_C)|\,, \tag{12}$$

where $C(\omega)$ is prescribed by the device dynamics, as indicated below equation (10), and $\mathcal{F}_C$ is the reactive part of the actuator force limit. The total force limit $\mathcal{F}_{lm}$ for the actuator system can be expressed as,

$$\mathcal{F}_{lm} = \sqrt{\mathcal{F}_R^2 + \mathcal{F}_C^2}. \tag{13}$$

Because this is a frequency-domain limit based on frequency-domain amplitudes, satisfaction of this constraint in the time-domain is not guaranteed. In the time domain, for irregular waves, it would be necessary to ensure that the sum of the two components, resistive and reactive, as evaluated in real time, is smaller than the force limit $\mathcal{F}_{lm}$. Actuator safety may require that such a check be performed at each instant.

The frequency-domain velocity constraint can be expressed as,

$$\begin{aligned} & U_r^2 \leq \beta_r^2, \quad U_i^2 \leq \beta_i^2 \\ & \Rightarrow \left(U_r^2 + U_i^2\right) \leq \left(\beta_r^2 + \beta_i^2\right), \\ & \Rightarrow UU^* \leq \beta\beta^* \end{aligned} \tag{14}$$

where * denotes complex conjugate, and the parentheses showing frequency dependence have temporarily been dropped for compactness. In terms of the actuator force components, the mean converted power and maximum reactive power can be expressed as,

$$\begin{aligned} P_w(\omega) &= \frac{1}{2} \left|F_{L1}(i\omega)\right| \left|U(i\omega)\right|, \\ P_a(\omega) &= \left|F_{L2}(i\omega)\right| \left|U(i\omega)\right|. \end{aligned} \tag{15}$$

Limiting of the force and velocity thus also allows the converted power and reactive power to be constrained.

A frequency-domain performance index may now be expressed as,

$$\begin{aligned} \overline{P}_w = & \frac{1}{4}\left[F_f^*(i\omega)U(i\omega) + F_f(i\omega)U^*(i\omega)\right] - \frac{1}{2}U^*(i\omega)b(\omega)U(i\omega) \\ & - \frac{1}{2}\lambda_1\left(U_r^2 - \beta_r^2\right) - \frac{i}{2}\lambda_2\left(U_i^2 - \beta_i^2\right), \end{aligned} \tag{16}$$

where λ_1 and λ_2 form the two Lagrange multipliers referred to earlier. The necessary condition for a stationary value of $\overline{P}_w$ can be expressed as, $\delta\overline{P}_w = 0$, which leads to the conditions,

$$\begin{aligned} & \frac{\partial\overline{P}_w}{\partial U} = 0; \quad \frac{\partial\overline{P}_w}{\partial U^*} = 0; \\ & \frac{\partial\overline{P}_w}{\partial \lambda_1} = 0; \quad \frac{\partial\overline{P}_w}{\partial \lambda_2} = 0. \end{aligned} \tag{17}$$

The third and fourth conditions in equation (17) simply lead to the envelope,

$$U_r^2 = \beta_r^2, \quad U_i^2 = \beta_i^2 \Rightarrow UU^* = \beta\beta^* \tag{18}$$

The first equation in (17) results in a condition to be satisfied by the complex conjugates of the quantities related together by the second equation in (17),

$$\frac{\partial\overline{P}_w}{\partial U^*} = \frac{1}{4}\left[F_f(i\omega)\right] - \frac{1}{2}\left[b(\omega) + \lambda_1(\omega) + i\lambda_2(\omega)\right]U(i\omega) = 0. \tag{19}$$

Equation (19) thus provides,

$$U(i\omega) \equiv U_o(i\omega) = \frac{F_f(i\omega)}{2\left[b(\omega) + \lambda_1(\omega) + i\lambda_2(\omega)\right]}. \tag{20}$$

Here $U_o(i\omega)$ denotes the constrained optimum velocity. It should be noted that, the optimum $U(i\omega)$ according to equation (20) is not purely in phase with the exciting force $F_f(i\omega)$. The approach followed above thus enables both an amplitude and a phase constraint on the device velocity. Effectively, the introduction of a phase constraint enables the device to be 'detuned' off the optimum, so that the oscillation amplitude, actuator forces, and the resistive and reactive powers can be within prescribed limits.

On the velocity envelope,

$$\lambda_1 + i\lambda_2 = \frac{F_f(i\omega)}{2\beta(i\omega)} - b(\omega). \tag{21}$$

Thus,

$$\begin{aligned} \lambda_1(\omega) &= \Re\left(\frac{F_f(I\omega)}{2\beta(i\omega)}\right) - b(\omega), \\ \lambda_2(\omega) &= \Im\left(\frac{F_f(i\omega)}{2\beta(i\omega)}\right). \end{aligned} \tag{22}$$

If, θ_f is used to define the prescribed phase difference limit between $F_f(i\omega)$ and $\beta(i\omega)$,

$$\begin{aligned} \lambda_1(\omega, \theta_f) &= \left|\frac{F_f(i\omega)}{2\beta(i\omega)}\right| \cos\theta_f - b(\omega), \\ \lambda_2(\omega, \theta_f) &= \left|\frac{F_f(i\omega)}{2\beta(\omega)}\right| \sin\theta_f. \end{aligned} \tag{23}$$

The phase angle θ_f may be chosen to be small, and prescribed such that λ_2 has a net subtractive effect on the reactive load $-C$. It may be convenient to use a small constant value for θ_f for a small device with a resonant period smaller than most energy periods expected. It can be seen that when $\theta_f = 0$, the constraint velocity is fully in phase with the exciting force, and $\lambda_2 = 0$. It can be seen further that, when $\theta_f \neq 0$ (since $|\cos\theta_f| < 1$, $\sin\theta_f \neq 0$, for $0 < \theta_f < \pi$),

$$\lambda_1(\omega, \theta_f) < \lambda_1(\omega, 0), \quad |\lambda_2(\omega, \theta_f)| > |\lambda_2(\omega, 0)| = 0. \tag{24}$$

The two force components then satisfy,

$$\begin{aligned} &\left[b(\omega) + \lambda_1(\omega, \theta_f)\right] |\beta(i\omega)| < \left[b(\omega) + \lambda_1(\omega, 0)\right] |\beta(i\omega)|, \\ &\left|\left[C(\omega) - \lambda_2(\omega)\right]\right| |\beta(i\omega)| < |C(\omega)|\, |\beta(i\omega)|. \end{aligned} \tag{25}$$

The right sides of the two equations (25) are the resistive and reactive force magnitudes without the phase-match constraint θ_f. Equations (25) therefore indicate that the present detuning approach would reduce the resistive and reactive forces required over the situation with no phase-match constraint. It can be noted that the four conditions expressed in equations (11), (12), (23) constrain the power take-off/device velocity and power take-off force components. These four conditions can be used to provide explicit values on the velocity and force envelopes (for a chosen θ_f). It is likely however that F_R and F_C will be constant magnitudes in practice, just as the displacement stroke α would be $|i\omega\alpha| = |\beta(i\omega)|$. Therefore, a semi-iterative approach may be preferred in practice, where the actuator system provides the best match with the force and displacement (velocity) constraints over most of the expected frequency range for the device.

In equations (20)–(23), introducing a frequency-response function $H_f(i\omega)$ such that

$$F_f(i\omega) = H_f(i\omega)A(i\omega), \tag{26}$$

a constrained optimum velocity response function can be defined as,

$$H_o(i\omega) = \frac{H_f(i\omega)}{2\left(b(\omega) + \lambda_1(\omega) + i\lambda_2(\omega)\right)}. \tag{27}$$

If a linearized viscous friction damping term c_d were to be added, $H_o(i\omega)$ could be redefined as,

$$H_o(i\omega) = \frac{H_f(i\omega)}{2\left(b(\omega) + c_d + \lambda_1(\omega) + i\lambda_2(\omega)\right)}. \tag{28}$$

In contrast, the frequency response function with the actuators applying a purely resistive load D would be (with $\lambda_1 = 0, \lambda_2 = 0$),

$$H_r(i\omega) = \frac{H_f(i\omega)}{b(\omega) + c_d + D + iC(\omega)}, \tag{29}$$

where $C(\omega)$ is the device reactance as defined in equation (10). The response in equation (29) occurs when only D can be adjusted over longer time scales by the power take-off, while the response in equation (28) is produced when the power take-off applies a damping load λ_1 in addition to $b(\omega)$, and subtracts λ_2 from the reactive load it applies. An impulse response function for constrained optimum response can now be expressed as,

$$h_o(t) = \frac{1}{2\pi}\int_{-\infty}^{\infty} H_o(i\omega)\mathrm{e}^{i\omega t}d\omega. \tag{30}$$

The constrained optimum velocity $u_o(t)$ in the time domain can now be found using,

$$u_o(t) = \int_{-\infty}^{\infty} h_o(\tau)\eta(x_B, t-\tau)d\tau, \tag{31}$$

where $\eta(x_B, t)$ denotes the incident wave surface elevation at the device centroid x_B. $h_o(t)$ is non-causal, i.e., $h_o(t) \neq 0$, $t < 0$. Hence $\eta(x_B, t)$ needs to be predicted as far into the future as h_o has memory into the past (see, for instance, [26]).

It should be noted that $F_f(i\omega)$ in equations (2) and (16) is exciting force per unit wave amplitude. The velocity (displacement) should therefore be constrained to be $\leq i\omega\alpha/A$ ($\leq \alpha/A$). In an irregular spectrum A varies with frequency ω, and it may be convenient, though by no means sufficient, for instance, to use an amplitude such as $H_{1/10}/2$, where $H_{1/10}$ is the average of 1/10 th highest waves in the spectrum.

It should be noted further that satisfaction of the constraints on a frequency-by-frequency basis (i.e. in the frequency domain) does not automatically imply constraint satisfaction in the time domain. In practice, hard end stops may be provided to limit device excursion and actuation displacement. The following section addresses the effect of end-stop impacts resulting from the present approach.

3. Effect of End-Stop Impacts

Although hard end-stops serve to limit oscillation strokes, each hard-stop impact potentially can excite an array of structural vibration modes as well as repeated damped oscillations of the device at its natural frequencies. End stops can thus have a deleterious effect on the device structure (e.g. by shortening its fatigue life) and a potential effect on the device conversion efficiency under a chosen control approach. For these reasons, considerable design effort was dedicated during the nineties to approaches to avoid them or to implement them 'softly' [22]. The goal here is just to understand the effect of hard stop impacts on energy conversion by the single-mode device above under constrained wave-by-wave impedance matching control. For simplification, it is helpful to distinguish between 'primary impacts' caused by large displacements due to wave-device dynamics, and 'secondary impacts' caused by large rebounds following an initial primary impact. Just the primary impacts are considered below, assuming that sufficient passive damping is provided at the end stops. It is also helpful to begin with the equation of motion in the time domain for a single-mode

device [27],

$$[m + \overline{a}(\infty)]\,\dot{u} + \int_0^\infty h_r(\tau)u(t-\tau)d\tau + c_d u + \int_{-\infty}^t ku(\tau)d\tau = F_f(t) - F_L(t). \tag{32}$$

where, as described in Section 2, F_f is the exciting force and F_L is the force applied by the actuator system. It is assumed that the actuator electronics enable it to 'zero' the force F_L just before the full impact (this could be enabled, for instance, by a contact switch or a laser interrupt.). Introducing a force term $F(t)$ defined as,

$$F(t) \doteq F_f(t) - F_L(t^-) - \int_0^\infty h_r(\tau)u(t-\tau)d\tau - c_d u - \int_{-\infty}^t ku(\tau)d\tau, \tag{33}$$

$$[m + \overline{a}(\infty)]\,\dot{u} = F(t). \tag{34}$$

It should be noted that for the 2-body axisymmetric system studied in this work, the inertia term $m + \overline{a}(\infty)$ is replaced by an equivalent mass, as summarized in Appendix 1. $F(t)$ is thus the total external force acting on the moving body that is balanced by the inertial force term on the left side of equation (34). At an end-stop impact, an equal and opposite force is generated at the end-stop, lasting only through the duration of the impact. Therefore, the motion of the body following the impact can be described by,

$$[m + \overline{a}(\infty)]\,\dot{u} = F(t) - F(t)\delta(t - t_n), \tag{35}$$

where $t = t_n$ denotes the time instant of impact, and $\delta(t)$ is the Dirac delta function modeling an instantaneous action. The viscous friction damping term c_d is assumed to be small. The control/actuator force $F_L(t^+) \neq 0$ just after the body begins its recoil from impact ($F_L(t) = 0$ only from t_n^- to t_n^+). Under wave-by-wave impedance matching control (see, for instance, [17]), with the force/velocity constraints applied as discussed in Section 2, normally,

$$u_o(t) = \int_{-\infty}^\infty h_{of}(\tau)F_f(t-\tau)d\tau, \tag{36}$$

in the absence of end-stop collisions. Here, h_{of} is defined such that,

$$h_{of}(t) = \frac{1}{2\pi}\int_{-\infty}^\infty \frac{1}{2\left(b(\omega)\lambda_1 + i\lambda_2\right)} \mathrm{e}^{i\omega t} d\omega \tag{37}$$

After a single end-stop impact,

$$u_{on}(t) = u_o(t) + u_{es}(t), \tag{38}$$

where $u_{es}(t)$ can be written as,

$$u_{es}(t) = \int_{-\infty}^{\infty} h_{of}(\tau)F(t-\tau)\delta(t-t_n-\tau)d\tau. \tag{39}$$

With the Dirac-delta function is centered on $\tau = t - t_n$,

$$u_{es}(t) = h_{of}(t-t_n)F(t_n). \tag{40}$$

so that,

$$u_{on}(t) = \int_{-\infty}^{\infty} h_{of}(\tau)F_f(t-\tau)d\tau + h_{of}(t-t_n)F(t_n). \tag{41}$$

When multiple impacts occur, the overall velocity can be estimated using,

$$u_{oe}(t) = \int_{-\infty}^{\infty} h_{of}(\tau)F_f(t-\tau)d\tau + \sum_{n=1}^{N} h_{of}(t-t_n)F(t_n). \tag{42}$$

As seen from equation (42), h_{of} operates on the exciting force $F_f(t)$ in the first term and on the force $F(t)$ (with $c_d = 0$) as expressed in equation (33). The converted time-averaged power with N end-stop impacts can be computed using the full velocity u_{oe} as,

$$P_{oe} = \frac{1}{T}\int_0^T F_L(t)u_{oe}(t)dt. \tag{43}$$

The converted power can be expressed as,

$$P_{oe} = P_o + P_e, \tag{44}$$

where,

$$P_o = \frac{1}{T}\int_0^T F_L(t)u_o(t)dt, \quad P_e = \frac{1}{T}\int_0^T F_L(t)u_e(t), \tag{45}$$

where,

$$u_e(t) = \sum_{n=1}^{N} h_{of}(t-t_n)F(t_n). \tag{46}$$

It is straightforward in the frequency domain to draw broad inferences about the effect of end-stop impacts on the amount of power converted. Noting that,

$$U_o(i\omega) = \frac{F_f(i\omega)}{2\left[b(\omega) + \lambda_1(\omega) + i\lambda_2(\omega)\right]}, \tag{47}$$

the Fourier transform of $u_e(t)$ as expressed in equation (46) is,

$$U_e(i\omega) = \sum_{n=1}^{N} \frac{F(t_n)\mathrm{e}^{-i\omega t_n}}{2\left[b(\omega) + \lambda_1(\omega) + i\lambda_2(\omega)\right]}. \tag{48}$$

The exponential $e^{-i\omega t_n}$ represents the memory effect of the nth collision. The converted power due to velocity $U_o(i\omega)$ and actuation force $F_L(i\omega)$ can be expressed as,

$$P_o(\omega) = \frac{1}{2}\Re\left[F_L^*(i\omega)U_o(i\omega)\right] = \frac{1}{2}\left[b(\omega) + \lambda_1(\omega)\right]U_o(i\omega)U_o^*(i\omega), \tag{49}$$

with just the resistive part of the force $F_L(i\omega)$ contributing to power conversion. In the presence of end-stop impacts,

$$P_{oe}(\omega) = \frac{1}{2}\left[b(\omega) + \lambda_1(\omega)\right]U_{oe}(i\omega)U_{oe}^*(i\omega), \tag{50}$$

where,

$$U_{oe}(i\omega) = U_o(i\omega) + U_e(i\omega). \tag{51}$$

With some algebra, it can be seen that,

$$P_{oe}(\omega) = P_o(\omega) + P_e(\omega) + Peo(\omega), \tag{52}$$

where $P_o(\omega)$ is as given by equation (49). $P_e(\omega)$ and $P_{eo}(\omega)$ are,

$$P_e(\omega) = \frac{1}{2}\left[b(\omega) + \lambda_1(\omega)\right]U_e(i\omega)U_e^*(i\omega);\ \text{and}\ P_{eo}(\omega) = \left[b(\omega) + \lambda_1(\omega)\right]\Re\left[U_o(i\omega)U_e^*(i\omega)\right]. \tag{53}$$

The term on the left in equation (53) is always greater than zero when $U_e(i\omega) \neq 0$, and adds to the converted power. The term on the right can be negative and can quantify loss of power conversion. Therefore, it can be inferred that P_e is negative and reflects loss of power when,

$$\Re\left[U_o(i\omega)U_e^*(i\omega)\right] < -\frac{1}{2}U_e(i\omega)U_e^*(i\omega). \tag{54}$$

It is important to note that the time-domain calculations based on equations (44) and (45) are direct, and do not need these arguments (which, though helpful in providing insight, may or may not hold at each time instant).

4. Calculations and Results

The formulation above is applied to an example situation here. Calculations are carried out for the device geometry shown in Figure 1. The buoy dimensions are modeled after a mid-size oceanographic buoy, with radius $R = 1.2$m, and the converted power is utilized to support oceanographic instrumentation. For this work, the draft is taken to be $D_r = 1.0$m. The two discs under the buoy are solidly connected and power conversion is through the relative heave oscillation between the buoy

and the reaction discs. Mass of any instrumentation supported between the two discs is not included in these calculations.

Simulations were carried out for wave conditions at a point in the Nantucket Shoals, off the U.S. East Coast (40.5N, 69.24W, water depth 74m) as recorded by the NDBC 44008 data buoy, which is close to the site of the *Pioneer array* Ocean Observatories Initiative deployment site [24]. The period June 18 to June 23, 2018 was selected as representative of average summer-time wave conditions at the site. The H_s (significant wave height) and T_e (energy period) combinations are shown in Figure 2. In the data used, the energy periods T_e range from 3s to 15s, and the significant wave heights H_s range from 0.7m to 2.1m. The maximum and minimum wave heights targeted for conversion would in general require closer coordination with designers of the overall system. The wave elevations for these sea states are synthesized by fitting a Pierson-Moskowitz spectrum to each H_s-T_e combination. Uni-directional, long-crested waves were assumed, so that,

$$S(\omega) = \frac{131.5 H_s^2}{T_e^4 \omega^5} \exp\left[-\frac{1054}{(T_e\omega)^4}\right]. \tag{55}$$

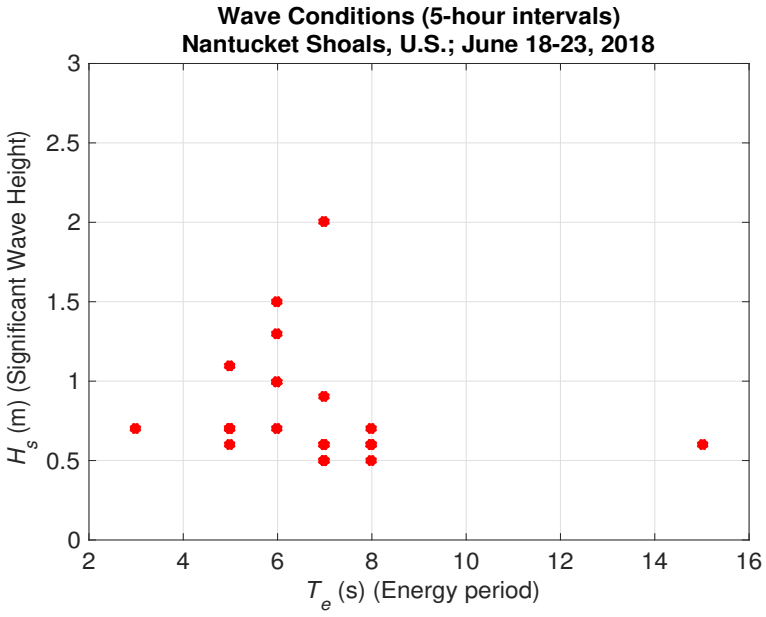

Figure 2: Plot showing the energy period and significant wave height combinations observed at the site off the U.S. east coast.

The wave elevation at a point x_A up-wave of the device was expressed as,

$$\eta(x_A;t) = \sum_{n=1}^{N} \Re\left\{A(\omega_n)\exp\left[-i\left(k(\omega_n)x_A - \omega_n t + \theta_n\right)\right]\right\}, \tag{56}$$

where,

$$A(\omega_n) = \sqrt{2S(\omega_n)\Delta\omega}, \tag{57}$$

and θ_n is a random number $\in [0, 2\pi]$, with $S(\omega_n)$ representing the spectral density value at ω_n. The wave elevation at the model location x_B was predicted at a time $t_p = 30$s into the future, using the expression,

$$\eta(x_B;t) = \int_{-\infty}^{\infty} h_l(\tau)\eta(x_A;t-\tau)d\tau, \tag{58}$$

where h_l is found as summarized in Appendix 2, and discussed in [26], [28], and [17], [29], [30], etc.

While the formulation in Sections (2) and (3) is described in terms of a single-mode device, the device used in the present work is a 2-body device, for which the equations of motion for heave oscillation of the two bodies can be reduced to a single equation for the relative heave oscillation, as discussed in [31] and used the work of [17] (and as summarized in Appendix 1). The hydrodynamic coefficients used for the two bodies were derived from [19]. As in [23] actuation was chosen here to be via hydraulic cylinders. The effect of mooring cables on the device stiffness was ignored. For the present simulations, hard end-stops on relative heave oscillation were set at ± 2.0m, while the phase-match limit was set at ± 0.43 rad. Calculations here were carried out for the set of sea states shown in Figure 2. As in [17], the average converted power [see also equation (45)] and the maximum reactive power in the time domain were found using,

$$\begin{aligned} P_w &= \frac{1}{T}\int_0^T F_{L1}(t)u_o(t)dt, \\ P_a &= \max_{0<t\leq T}\left[F_{L2}(t)u_o(t)\right], \end{aligned} \tag{59}$$

where $T \geq 600$s, and P_w may be P_o or P_{oe} from equation (45).

Figures 3–7 plot the time-domain results for a chosen sea-state, $H_s = 1.0$m, $T_e = 6.0$s. Shown in these plots are the predicted wave profiles used in this work, the converted power, relative heave displacement between buoy and discs, the resistive and reactive forces required of the actuators, relative heave velocity of the device following end-stop impacts, and converted power time series with end stop impacts occurring.

Figures 10–13 summarize the results over the sea-states considered here, with and without end-stop impacts. These results plot converted power means (over 30 min), and the 30-min maximum relative displacement, force, and reactive power.

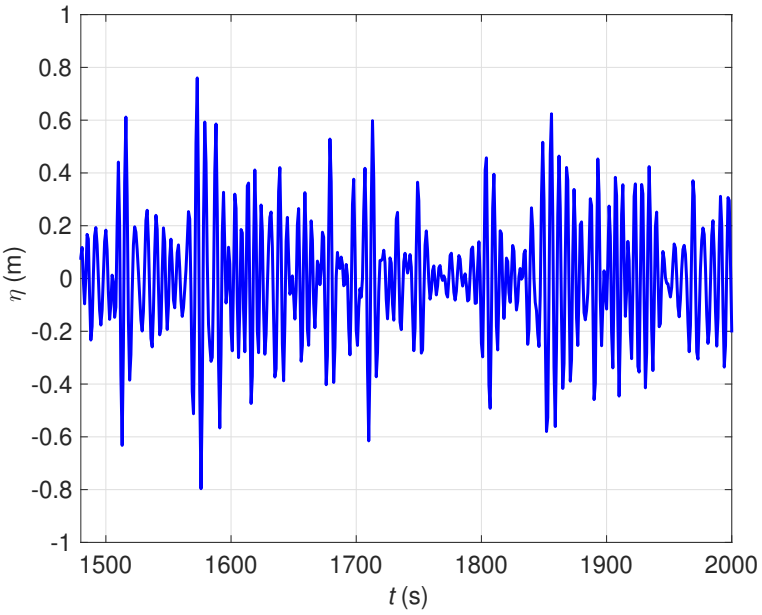

Figure 3: The predicted wave elevation time series for the test conditions ($H_s = 1.0$m, $T_e = 6.0$s) at prediction time $t_p = 30$s, obtained as summarized in Appendix 2.

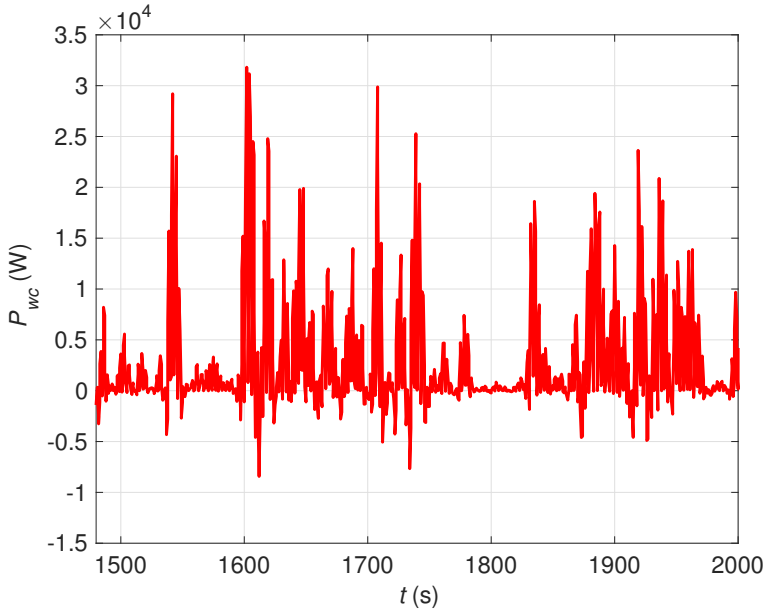

Figure 4: The converted power time series for the test conditions (H_s = 1.0m, T_e = 6.0s) with the amplitude and phase-limit conditions as applied here.

Results are discussed more fully in section 5.

5. Discussion of Results

The wave elevation record of Figure 3 is the predicted wave profile with a prediction time of 30s as desired for the coupled heave dynamics of the device. It should be pointed out that a reasonable agreement was found between predicted and actual wave elevation time histories (with root-mean-square errors $\sim$ 7%) for computer-generated waves [17], and the technique is currently being evaluated in wave tank and at-sea testing. The converted power time series for the wave record in Figure 3 is shown in Figure 4. As expected, large amounts of power are converted in response to the larger elevations. Also of interest to note are the short intervals of negative powers, which are a consequence of the intentional detuning caused by the phase constraint, as applied via λ_2 in equation (20) of Section 2 (since λ_2 keeps the relative heave velocity from directly being synchronous with the equivalent exciting force on the relative heave oscillation).

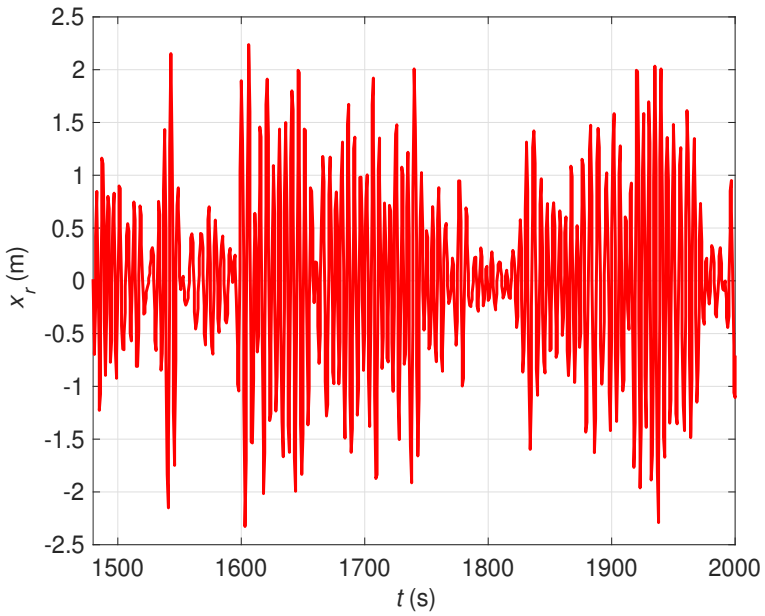

Figure 5: The relative heave displacement time series for the test conditions ($H_s = 1.0$m, $T_e = 6.0$s) with the amplitude and phase-limit conditions as applied here.

Figure 5 plots the relative heave displacement between the buoy and the discs. The increase and decrease in amplitude is seen to be consistent with the amplitude variations in the approaching wave groups. While the time series of this figure shows relative oscillations unobstructed by end stops, it should be pointed out that the relative heave amplitude here exceeds $\pm$2m at a few points, at which impacts would occur, were end-stops present. Because the displacement and force constraints are based on frequency domain arguments, constraint satisfaction in the time domain is not guaranteed. With the end-top impacts occurring at each instant the displacement limit is reached, the relative heave velocity in the time domain takes a form such as shown in Figure 6. As expected, following each impact are large rebound velocities and oscillations that get damped out over a length of time ($\sim$ 60s). The present calculations do not account for secondary self-sustaining repeated impacts due to rebound velocities alone, though this effect could be worth evaluating further, given its possible consequences for system stability in certain sea states. The present simplification was largely motivated by recent experimental studies on a 1/10 th scale model, where self-sustaining repeated rebounds were not observed [23]. The effect of end-stop impacts on converted power, as quantified under the present formulation is shown in Figure 7. The instantaneous power values shown here are power converted from the combined relative velocity (i.e. the original unobstructed velocity + the

velocity due to end-stop impacts). The plot shows the net effect of the combined velocity as given by equations (44), and (45), which can be additive or subtractive.

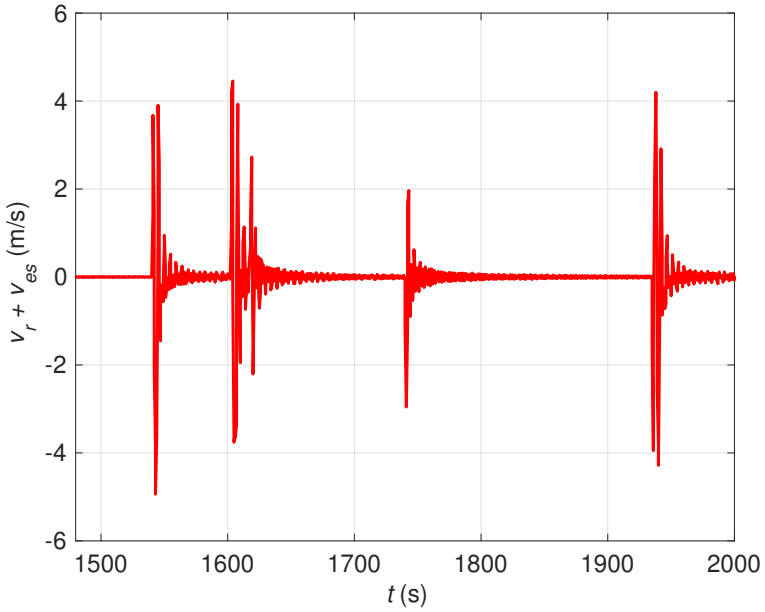

Figure 6: The relative heave velocity time series, as resulting from end-stop impacts for the test conditions ($H_s = 1.0$m, $T_e = 6.0$s) with the amplitude and phase-limit conditions as applied here. This is the time series without superimposing the wave-induced velocity time series.

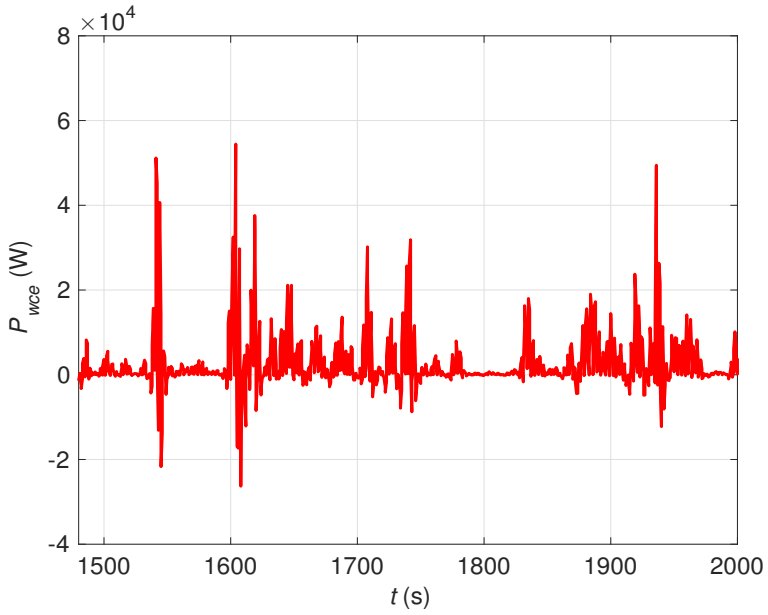

Figure 7: The converted power time series with end-stop impacts occurring, for the test conditions (H_s = 1.0m, T_e = 6.0s) with the amplitude and phase-limit conditions as applied here.

Figures 8 and 9 plot the resistive and reactive forces needed to provide the detuned impedance match sought in this paper. With the force limit set at ±100kN for the hydraulic actuators considered here, the force constraint is seen to be satisfied easily under the present amplitude and phase-match constraint approach.

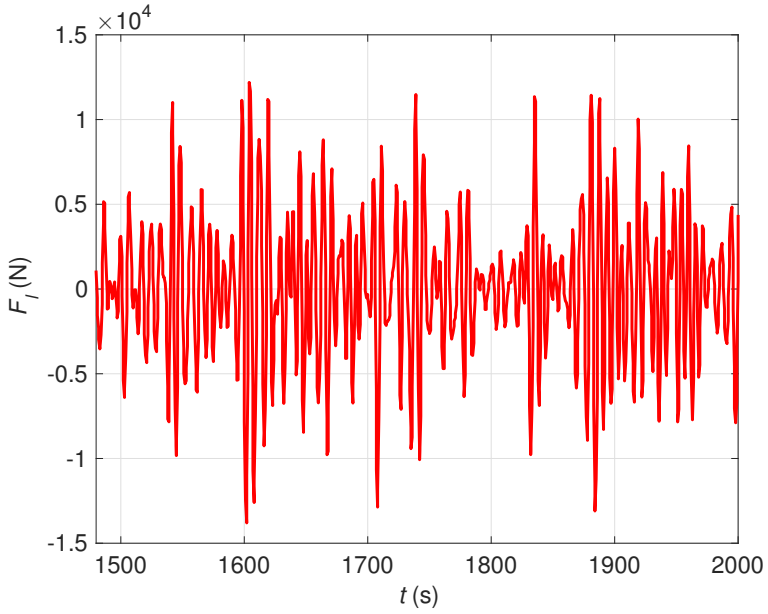

Figure 8: The resistive force time series required for the test conditions (H_s = 1.0m, T_e = 6.0s) with the amplitude and phase-limit conditions as applied here.

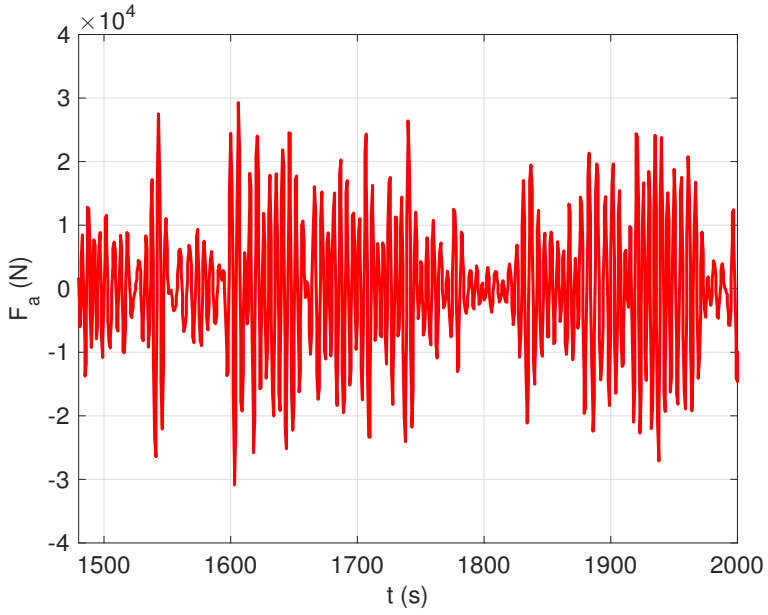

Figure 9: The reactive force time series required for the test conditions (H_s = 1.0m, T_e = 6.0s) with the amplitude and phase-limit conditions as applied here.

The next set of figures presents overview results for the chosen site in the Nantucket Shoals

area, off the U.S. East Coast (40.5N, 69.24W, water depth 74m). The 30-min mean power plot of Figure 10 shows the effect of the amplitude-phase constraints, in that the mean converted power under detuned impedance matching is considerably smaller than the incident wave power per unit crest length, for the more energetic sea states. However, the constrained capture width nearly approaches unity for some of the less energetic sea-states. This type of behavior represents the desired effect of the present constrained control on a small heaving device ($\sim$ 1.2m radius). Note that the theoretically maximum capture width here is $L_w/(2\pi)$, which of course would for this device would require unattainable actuator strokes and forces for impedance matching. Another notable aspect of Figure 10 is that the converted power with end stop collisions is only negligibly smaller than what it would be without the end-stop imposed hard limits. This is likely a result of the actuator converting a large portion of the oscillations following end-stop collisions into useful power. It is recalled that, in the frequency domain, the power converted from end-stop impacts is expected to be net negative when the inequality condition in equation (54) is met. It should be pointed out that secondary end-stop impacts are ignored, assuming that the coefficient of restitution at the end stops is sufficiently small.

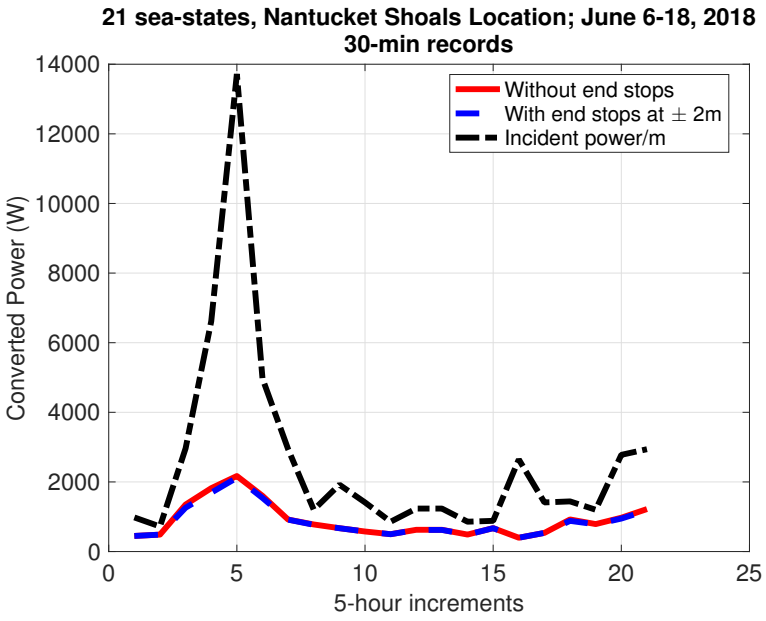

Figure 10: Overview of power conversion for the various sea-states tested in this work under amplitude and phase-limit conditions. Note that conversion is close to maximum in the less energetic spectra, as desired, while the constraints lead to a significantly smaller converted power relative to the average incident power.

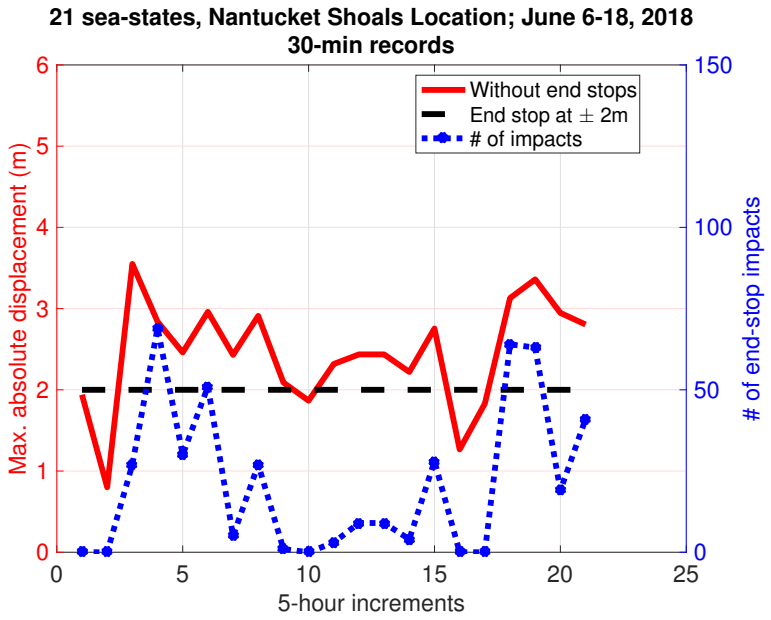

Figure 11: Overview of the 30-min maximum displacement in the various sea-states tested in this work under amplitude and phase-limit conditions. Also shown is the number of times end-stop collisions occur during each 30-min simulation.

Figure 11 plots the 30-min maxima for relative heave displacement amplitude. It is seen that the stroke limit is exceeded in several sea states. To clarify how frequently the chosen stroke limit was exceeded, also shown in the figure is the number of end-stop collisions during each 30-min simulation. For the present design/constraint choices, note that the end-stop collisions are only avoided in only some of the less energetic sea states. Given the potential risks associated with repeated secondary end-stop impacts (instability, free-vibration excitation at structural natural frequencies, fatigue, etc.), however, it would seem appropriate to revise actuator design choices suitably. It is recalled that the displacement constraints are determined by the maximum actuator stroke available, as many commonly used linear actuators would likely not allow peak-to-peak oscillations exceeding about 4m [32]. It is interesting to consider that larger device dimensions would alter the overall dynamics of the device, and would reduce the maximum relative displacements under equivalent levels of impedance-matching control. The required actuation/control force magnitudes (and overall device costs), on the other hand, may be greater. The effect of dimension changes would be of interest to investigate further in the wider context of wave energy devices, and for oceanographic measurement applications in which some dimensional flexibility is permissible.

Figure 12 plots the 30-min force maxima along with the force constraint of 100kN. It is observed

that the force constraint has been met in all cases. Overall, however, one could reduce the detuning phase offset at the expense of increased resistive force to meet the displacement constraint, so that greater power may be absorbed while possibly reducing the number of end-stop collisions. Alternative actuator designs providing greater strokes without loss of maximum force could also be evaluated for cost-effectiveness.

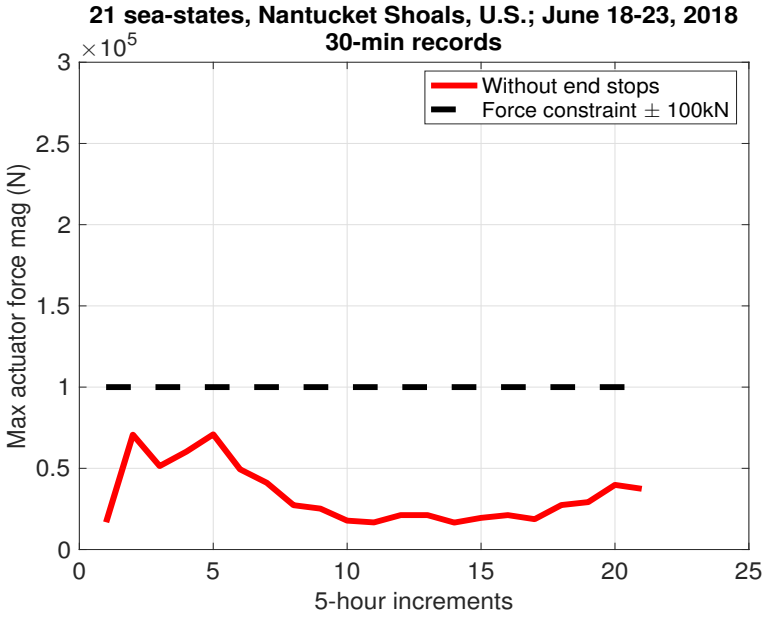

Figure 12: Overview of the 30-min maximum force in the various sea-states tested in this work under amplitude and phase-limit conditions. The forces are seen to be within the imposed constraints.

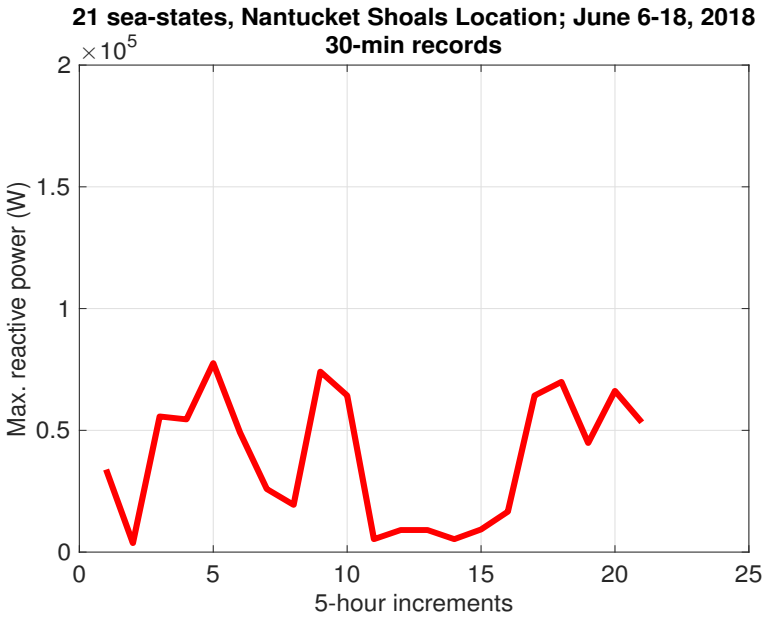

Figure 13: Overview of the 30-min maximum reactive power in the various sea-states tested in this work under amplitude and phase-limit conditions.

The maximum reactive power requirement is shown in Figure 13. It is encouraging that the maximum reactive power is less than 100 kW, perhaps thanks to the detuning effect of the phase-match limit. There thus appears to be scope for broader optimization of the power take-off design, over the range of force, displacement, resistive, and reactive power limits, where the best conversion efficiency and mechanical/structural design effectiveness can be approached closely. Note that the latter criterion plays a major role in determining the overall reliability of the device.

6. Conclusion

The goal of this paper was to investigate a technique for concurrent use of amplitude and phase-match constraints under constrained wave-by-wave impedance matching control based on predicted and past wave elevations at the body (see Appendix 2 for more details). The intentional detuning effect of this approach was designed to limit both oscillation stroke and actuation force required for control. The displacement limits were assumed to be defined by actuator stroke, which by design was chosen to be smaller than the body-motion limits (for instance, the smaller of draft and freeboard for heave oscillations). The constraining parameters were set within an analytical frequency domain formulation for operation over the allowed displacement/force envelopes. This technique does not

guarantee satisfaction in the time domain, however, so that collisions with hard end stops (provided to protect the actuator hardware) may occur. The effect of end-stop impacts on device velocity and converted power was considered. Self-sustaining repeated secondary rebounds between end stops were ignored, assuming that the end stop hardware is designed to provide a coefficient of restitution that is sufficiently smaller than unity.

Time domain simulation results were discussed for a range of wave conditions spanning 5 summer days off the U.S. East Coast at a site in the Nantucket Shoals area (40.5N, 69.24W, water depth 74m). This site is close to the deployment location of the *Pioneer array* system of moorings that form part of the Ocean Observatories Initiative deployments [24]. Under the conditions studied, the force constraint was met easily, while the displacement constraint was exceeded in several sea states, so that further optimization of the present device seems warranted. With the oscillations from end-stop impacts decaying stably, end-stop collisions were found to have little effect on the 30-min average converted power.

Further work should include optimization of the detuning parameter λ_2, force and displacement limits, and if permitted by the application, also the overall geometry design. As part of this study, a sensitivity analysis for the device dimensions such as buoy diameter, draft, and submergence of the reaction discs relative to dominant wave lengths may prove valuable. The present work could be of use in ensuring that the primary converter and power take-off systems are well matched for wave-by-wave impedance matching control, so that the device provides a large annual energy output at reasonable cost.

Acknowledgements

This work was made possible by a grant (# 1841361) from the U.S. National Science Foundation. I am grateful to Program Director Kandace Binkley for her interest and insightful feedback. It is a pleasure to thank Jean-Baptiste Richon of Laser Imaging Solutions, Ltd, Edinburgh, UK for collaborating on ongoing experimental work. Thanks are due also to the reviewers of this paper for their many helpful comments and suggestions.

The views expressed in this paper are those of the author and do not reflect the views and positions of the National Science Foundation or the U.S. Government.

References

[1] D. V. Evans. Power from water waves. *Annual Review of Fluid Mechanics*, 13:157–187, 1981.

[2] A.F.O. Falcao. Wave energy utilization: a review of the technologies. *Renewable and Sustainable Energy Reviews*, 14:899–918, 2010.

[3] S.H. Salter. Wave power. *Nature*, pages 720–724, June 1974.

[4] S.H. Salter. Recent progress on ducks. In *Proc. 1st Symposium on Wave Energy Utilization, Gothenburg, Sweden*, 1979.

[5] S. H. Salter. Progress on Edinburgh ducks. In D.V. Evans and A.F. de O. Falcão, editors, *Proc. IUTAM Symp. Hydrodynamics of Wave Energy Utilization*, pages 35–50. Springer Verlag, Berlin, 1985.

[6] K. Budal and J. Falnes. Optimum operation of improved wave power converter. *Marine Science Communication*, 3:133–150, 1977.

[7] S.H. Salter. Development of the duck concept. In *Proc. Wave Energy Conference*, 1978. Heathrow, U.K.

[8] K. Budal and J. Falnes. Interacting point absorbers with controlled motion. In B.M. Count, editor, *Power from Sea Waves*, pages 381–399. Academic Press, London, 1980.

[9] G.P. Thomas and D.V. Evans. Arrays of three-dimensional wave-energy absorbers. *Journal of Fluid Mechanics*, 108:67–88, 1981.

[10] D. Pizer. Maximum wave-power absorption of point absorbers under motion constraints. *Applied Ocean Research*, 15(4):227–234, 1993.

[11] J. Falnes. Maximum wave-energy absorption by oscillating systems consisting of bodies and water columns with restricted or unrestricted amplitudes. In *Proc. International Polar and Offshore Engineering Conference*, 2000. Seattle, USA.

[12] J. Hals, J. Falnes, and T. Moan. Constrained optimal control of a heaving buoy wave energy converter. *J. Offshore Mechanics and Arctic Engineering*, 133(1):1–15, 2011.

[13] J.A.M. Cretel, G. Lightbody, G.P. Thomas, and A.W. Lewis. Maximization of energy capture by a wave-energy point absorber using Model Predictive Control. In *Proc. 18th IFAC World Congress*, 2011. Milano, Italy, September 2011, preprint.

[14] R.G. Coe, G. Bacelli, S.J. Spencer, and H. Cho. Initial results from wave tank tests of close-loop wec control. Technical report, Sandia National Laboratories, Novermber 2018. SAND2018-12858.

[15] G. Bacelli and J.V. Ringwood. A geometrical interpretation of force and position constraints in the optimal control of wave energy devices. In *Proc. 9th European Wave and Tidal Energy Conference*, 2011. Southampton, UK.

[16] U.A. Korde and J.V. Ringwood. *Hydrodynamic Control of Wave Energy Devices*. Cambridge University Press, Cambridge, UK, 2016.

[17] U.A. Korde. Near-optimal control of a wave energy device using deterministic-model driven incident wave prediction. *Applied Ocean Research*, 53:31–45, 2015.

[18] U.A. Korde, J.Y. Lyu, R.D. Robinett, D.G. Wilson, G. Bacelli, and O. Abdelkhalik. Constrained near-optimal wave-by-wave control of a wave energy device in three oscillation modes. *Applied Ocean Research*, 69:126–137, 2017.

[19] U.A. Korde, J.J. Song, R.D. Robinett, and O. Abdelkhalik. Hydrodynamic considerations in near-optimal control of a wave energy converter for ocean measurement applications. *Marine Technology Society Journal*, 51(6):44–57, 2017.

[20] S. H. Salter. Wave energy: Nostalgic ramblings, future hopes and heretical suggestions. *J. Ocean Engineering and Marine Energy*, 2(4):399–428, November 2016.

[21] G. Fredrikson. IPS wave power buoy mark IV. In *Wave Energy Research and Development Workshop*, 1992. Cork, Ireland.

[22] S.H. Salter and C.P. Lin. Wide tank efficiency measurements on a model of the sloped IPS buoy. In *Proc. 3rd European Wave Energy Conference*, Patras, Greece, 1998.

[23] U.A. Korde and J.B. Richon. Recent experimental testing of a 2-body wave energy converter under wave-by-wave impedance matching control. Technical report to the National Science Foundation, U.S., 2018.

[24] OOI. Ocean observatories initiative. https://oceanobservatories.org/technical-data-package/.

[25] K. Budal. Floating structure with heave motion reduced by force compensation. In *Proc. ASME Offshore Mechanics and Arctic Engineering Conference*, pages 92–101, 1985.

[26] J. Falnes. On non-causal impulse response functions related to propagating water waves. *Applied Ocean Research*, 17(6):379–389, 1995.

[27] W. Cummins. The impulse response function and ship motions. Technical report, David Taylor Model Basin DTNSRDC, 1962.

[28] M.R. Belmont, J.M.K. Horwood, R.W.F Thurley, and J. Baker. Filters for linear sea-wave prediction. *Ocean Engineering*, 33(17–18):2332–2351, 2006.

[29] M. R. Belmont, J. Christmas, J. Dannenberg, T. Hilmer, J. Duncan, J. M. Duncan, and B. Ferrier. An examination of the feasibility of linear deterministic sea wave prediction in multidirectional seas using wave profiling radar: Theory, simulation, and sea trials. *J. Atmospheric and Oceanic Technology*, 31:1601–1614, 2014.

[30] M. Al-Ani, J. Christmas, and M.R. Belmont. Deterministic sea-waves prediction using mixed space-time radar wave data. *Journal of Atmospheric and Oceanic Technogy*, 36:834–841, 2019.

[31] J. Falnes. Wave-energy conversion through relative motion between two single-mode oscillating bodies. In *Proc. ASME Offshore Mechanics and Arctic Engineering Conference*, July 1998. Lisbon, Portugal.

[32] J. Bard and P. Kracht. Linear generator systems for wave energy converters. Technical report, Fraunhofer IWES and Aalborg University, September 2013. www.sdwed.civil.aau.dk/digitalAssets/97/97525_d3.2.pdf.

[33] J. N. Newman. *Marine Hydrodynamics*. MIT Press, Cambridge, 1978. Second Printing, Call No. (VM 156.N48)., ix + 402 pp.

Appendix 1: 2-Body Axisymmetric Device with Concentric Buoy and Submerged Discs

As described in [17] and [19], the frequency domain model for the present 2-body device can be written as

$$\begin{aligned}
&\left[Z_t(i\omega) + Z_L(i\omega)\right] v_t(i\omega) + i\omega \left[Z_c(i\omega) - Z_L(i\omega)\right] v_b(i\omega) = F_{ft}(i\omega) \\
&\left[Z_c(i\omega) - Z_L(i\omega)\right] v_t(i\omega) + \left[Z_b(i\omega) + Z_L(i\omega)\right] v_b(i\omega) = F_{fb}(i\omega)
\end{aligned} \tag{60}$$

where the matrix elements are defined as,

$$\begin{aligned}
Z_t(i\omega) &= i\omega \left[m_t + \overline{a}_t(\infty) + a_t(\omega)\right] + \frac{k_t}{i\omega} + \left(c_{dt} + b_{dt}(\omega)\right) \\
Z_b(i\omega) &= i\omega \left[m_b + \overline{a}_b(\infty) + a_b(\omega)\right] + \frac{k_b}{i\omega} + \left(c_{db} + b_{db}(\omega)\right) \\
Z_c(i\omega) &= i\omega a_c(\omega) + b_c(\omega) \\
Z_L(i\omega) &= L(\omega) + \frac{N(\omega)}{i\omega}
\end{aligned} \tag{61}$$

Where the letter m is used to denote in-air mass with the subscripts t and b respectively denoting the top and bottom bodies. b_{dt} and b_{db} denote the frequency-dependent radiation damping for the two bodies, while $\overline{a}_t(\infty)$ and $\overline{a}_b(\infty)$ denote the infinite-frequency added masses for the two bodies and $a_t(\omega)$ and $a_b(\omega)$ represent just the frequency-dependent parts of the respective added masses. The letter k denotes stiffness (hydrostatic for the floating buoy and mooring-related for the submerged disc), while c_{dt} and c_{db} represent the linearized viscous damping coefficients. a_c and b_c denote the frequency-variable added mass and radiation damping due to coupling between the two bodies. Z_L represents the load impedance applied by the power take-off on the relative oscillation. Following the approach of Falnes [31], it is possible to express equation (60) as a scalar equation in terms of the relative velocity $v_r(i\omega)$,

$$v_r(i\omega) = v_t(i\omega) - v_b(i\omega), \tag{62}$$

by defining,

$$\overline{Z}(i\omega) = Z_t(i\omega) + Z_b(i\omega) + 2Z_c(i\omega), \tag{63}$$

and

$$F_f(i\omega) = \frac{F_{ft}(i\omega)\left(Z_b(i\omega) + Z_c(i\omega)\right)}{\overline{Z}(i\omega)} - \frac{F_{fb}(i\omega)\left(Z_t(i\omega) + Z_c(i\omega)\right)}{\overline{Z}(i\omega)}. \tag{64}$$

it is seen that

$$v_r(i\omega) = \frac{F_f(i\omega)}{Z_i(i\omega) + Z_L(i\omega)}, \tag{65}$$

where

$$Z_i(i\omega) = \frac{Z(i\omega)Z_s(i\omega) - Z_c^2(i\omega)}{\overline{Z}(i\omega)}. \tag{66}$$

Figure 14 illustrates the equivalent radiation impedance of the coupled 2-body system. The reactance terms due to in-air mass and infinite-frequency added mass and the hydrostatic stiffness are not included in this plot because of their relatively large magnitudes. The equivalent-body radiation damping is found to decrease to zero with increasing frequency as expected. Similarly, the reactive term is seen to peak and then fall toward zero beyond $\omega \to 4.0$. There is an irregular frequency close to $\omega \to 4.5$ in the numerical results used for this work [19], however, and only results up to $\omega = 4.0$ are used in the calculations in this work.

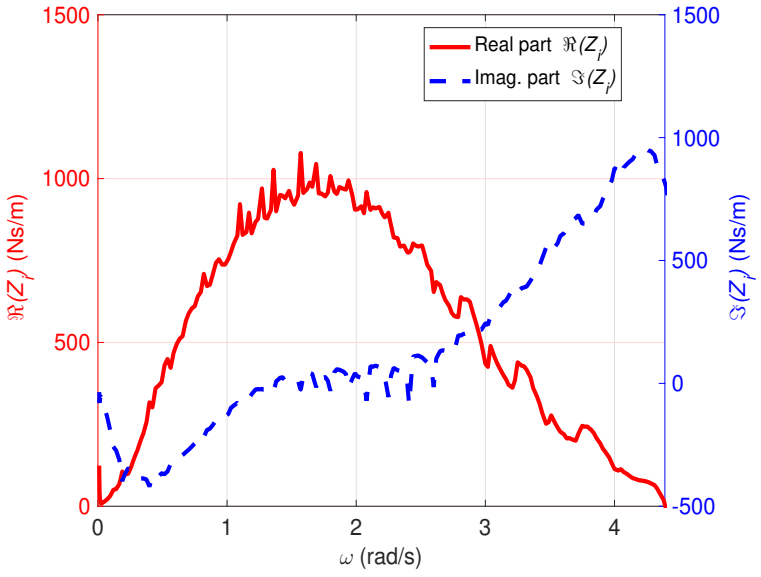

Figure 14: Intrinsic impedance real and imaginary components for the equivalent single-body representing the 2-body coupled axi-symmetric system. Contributions of the in-air mass, infinite-frequency added mass, and hydrostatic stiffness are not included. The rapid undulations are likely due to interpolation errors introduced because the frequency-increment in the original data from the software calculations [19] was greater than that used in the present work.

In the analysis of Section 2,

$$\begin{aligned} U(i\omega) &\leftarrow v_r(i\omega), \\ b(\omega) &\leftarrow \Re\left(Z_i(i\omega)\right), \\ C(\omega) &\leftarrow \Im\left(Z_i(i\omega)\right). \end{aligned} \tag{67}$$

It should be noted that linearized viscous damping has been ignored in most of the present analysis. For the analysis in Section 3, the inertia term $m + \overline{a}(\infty)$ is replaced by,

$$m + \overline{a}(\infty) \leftarrow \frac{(m_t + \overline{a}_t(\infty))\,(m_b + \overline{a}_b(\infty))}{(m_t + \overline{a}_t(\infty) + m_b + \overline{a}_b(\infty))}. \tag{68}$$

Appendix 2

The control technique used in this work requires wave profile prediction as far ahead as the radiation impulse response function has memory in the past (about 30 s in this work). The overall technique as described in [28], [26], and developed further in [17] is summarized below for completeness. The prediction model is kinematic, assumes long-crested waves in deep water. Prediction of multi-directional waves is discussed in [29]. It should be noted reliable prediction in multi-directional waves may require an approach that recognizes the finite time between successive spatial samples, as obtained, for instance, by a rotating radar. In such a case, a mixed space-time approach based on spectral coefficients may be needed [30].

It is assumed that there are periods of calm before and after the time period of interest, so that at any point x, $\eta(x,t) \to 0$ as $t \to \pm\infty$ [33], which enables Fourier transformability. In [17] the distance separating the point of measurement x_A and the point of prediction x_B was on the order of 1000m, and an advancing time series of surface elevation spanning about 260s was used to predict the wave elevation at the device centroid about 30s into the future. The prediction time was based on the heave radiation impulse response function for the device (particularly the time at which it could be truncated without serious loss of accuracy). In deep water, for uni-directional wave propagation, a kinematic model relating the wave elevation at point x_A to that at point x_B in the frequency domain can be expressed (with $d = x_B - x_A$) as

$$\eta(x_B; i\omega) = \mathrm{e}^{-ik(\omega)d}\eta(x_A; i\omega), \tag{69}$$

where $k(\omega)$ using the deep-water dispersion relation is

$$k(\omega) = \frac{|\omega|\omega}{g}. \tag{70}$$

$k(\omega)$ has the same sign as ω (which in the inverse Fourier transformation of equation (72) below ranges from $-\infty$ to ∞ for a full description of the time-domain function $h_l(t,d)$ below) . The wave elevation time history for predominantly uni-directional waves may be obtained by a non-directional

wave rider buoy. For most realistic surface wave spectra over which a wave energy device operates, ω may be expected to be within finite approximate limits ω_l and ω_h. Because surface waves are dispersive, an impulsive excitation of the wave surface propagates over a range of group velocities $[v_{gmn}, v_{gmx}]$, where, for deep water,

$$\begin{aligned} v_{gmn} &= \frac{1}{2}\left(\frac{g}{\omega_{mx}}\right) \\ v_{gmx} &= \frac{1}{2}\left(\frac{g}{\omega_{mn}}\right). \end{aligned} \tag{71}$$

The prediction at x_B using a measurement at x_A can be obtained using an impulse response function $h_l(t;d)$ where

$$h_l(t;d) = \frac{1}{2\pi}\int_{-\infty}^{\infty} \mathrm{e}^{-ik(\omega)d}\mathrm{e}^{i\omega t}d\omega \tag{72}$$

$h_l(t;d)$ can be evaluated analytically as [26], [28], and [17] as

$$\begin{aligned} h_l(t;d) =& \frac{1}{4}\sqrt{\frac{2g}{\pi d}}\left[\cos\left(\frac{gt^2}{4d}\right) + \sin\left(\frac{gt^2}{4d}\right)\right] \\ &+ \frac{1}{2}\sqrt{\frac{2g}{\pi d}}\left[\cos\left(\frac{gt^2}{4d}\right)\mathrm{C}\left(t\sqrt{\frac{g}{2\pi d}}\right)\right] \\ &+ \frac{1}{2}\sqrt{\frac{2g}{\pi d}}\left[\sin\left(\frac{gt^2}{4d}\right)\mathrm{S}\left(t\sqrt{\frac{g}{2\pi d}}\right)\right], \end{aligned} \tag{73}$$

where C and S denote the two Fresnel integrals. Using a wave surface-elevation time-series measurement at x_A over $[t-T, t]$ seconds, the surface elevation at $x_B = x_A + d$ at time $t + t_p$ can be obtained using

$$\begin{aligned} &\eta(x_B; t+t_p) = \int_0^T h_l(\tau)\eta(x_A; t-\tau)d\tau;\ t > T \\ &x_B - x_A = d = t_P v_{gmx} \\ &T = \frac{d}{v_{gmn}} - \frac{d}{v_{gmx}}. \end{aligned} \tag{74}$$

Further details and results are discussed in [17]. The technique is currently being tested using wave tank and at-sea wave profile measurements (but see in particular, [29]).